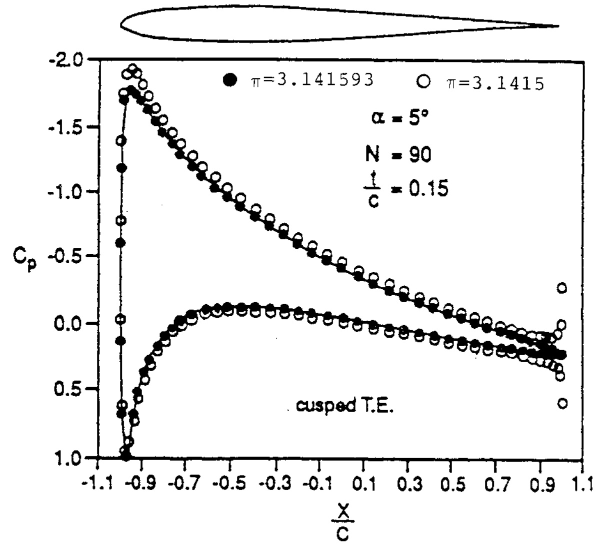

Fig. 1 Pressure distribution on an airfoil with a cusped trailing edge.

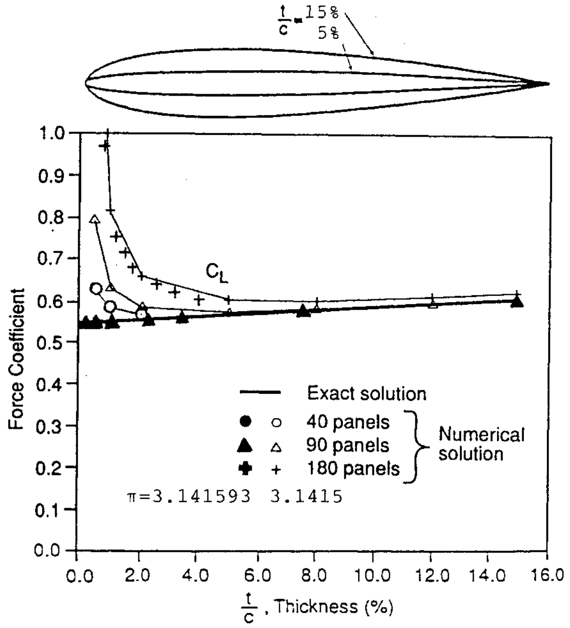

Fig. 2 Lift force vs airfoil thickness ratio.

predicted from linear analysis, Eq. (5), is 14% whereas Eq. (6) predicts an error of 16% based on a value of C of 0.55.

The lift coefficient is plotted vs airfoil thickness in Fig. 2 for airfoils with wedge trailing edges. The results for $\pi = 3.1415$ with 90 and 180 panels are indistinguishable from those of Ref. 3 and deviate markedly from theory for less than 5% thickness. The lift for 40 panels differs slightly from Ref. 3 because of error in integrating the pressure distribution. The more exact code is within 1% of the theoretical lift for the 40, 90, and 180 panel cases, including the thinnest airfoil indicated ($t/c = 0.25\%$, $h/a = 0.005$). The trailing-edge loading vs trailing-edge angle, Fig. 3, shows a consistent tendency for the original code to have positive loading from excessive circulation. The more exact code yields trailing-edge pressure differences near zero for the 40, 60, and 90 panel cases. Only the last is shown for clarity.

As seen in Fig. 2, for a thickness of 0.5% ($h/a = 0.01$) and 90 panels the error in π (−0.000093) in the original code produces an error in lift of 50%. This agrees with Eq. (6) given a value of C of 0.4 whereas Eq. (5) predicts 33%. For the corrected code ($\varepsilon/\pi = 10^{-7}$), the ratio $N/(h/a)$ must be less than approximately 80000 if the lift is to be accurate to 1%. For example, if 90 panels were used, the trailing-edge angle could be as small as 0.002 if all other calculations were exact.

VSAERO[4] (version E.4), a three-dimensional panel method used by the industry, was applied without special trailing-edge treatment to aspect ratio 20 wings, each with a cusped or wedge airfoil. Ten spanwise divisions were used with 90 chordwise panels. Lift and trailing-edge pressure difference at the wing centerline behaved the same as the more exact two-dimensional code for trailing-edge angles as low as 0.005. Sixteen spanwise divisions were needed for the 0.25% thick wedge airfoil to maintain the desired accuracy. Truncating π to 3.1415 increased the lift of the 1% thick wedge airfoil from 0.52 to 0.61 and trailing-edge loading from 0.01 to 0.96, close to the two-dimensional effect.

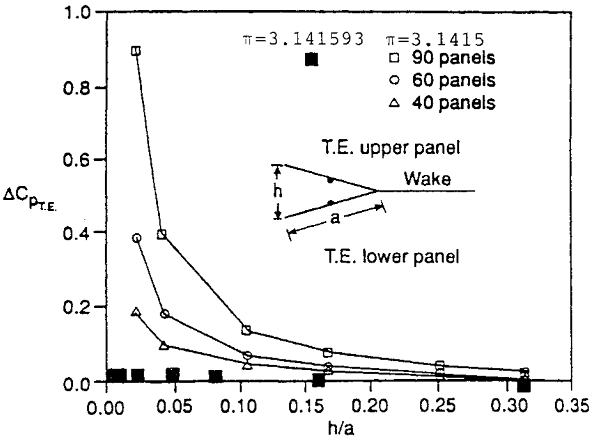

Fig. 3 Pressure difference between the trailing-edge upper and lower panels vs trailing-edge angle.

Potential-based panel methods require numerical precision in proportion to the ratio of the number of panels to the trailing-edge angle for accurate lift calculation. Based on results in two and three dimensions for airfoils with cusped and wedge trailing edges, it is concluded that single precision is sufficient for trailing-edge angles as low as 0.005. The problem studied in Ref. 3 is the result of imprecise specification of the value of π and is seldom encountered in computer codes used by the industry.

References

[1] Morino, L., and Kuo, C. C., "Subsonic Potential Aerodynamics for Complex Configurations: A General Theory," *AIAA Journal*, Vol. 12, No. 2, 1974, pp. 157–163.

[2] Katz, J., and Plotkin, A., *Low-Speed Aerodynamics: From Wing Theory to Panel Methods*, McGraw-Hill, New York, 1991.

[3] Yon, S., Katz, J., and Plotkin, A., "Effect of Airfoil (Trailing-Edge) Thickness on the Numerical Solution of Panel Methods Based on the Dirichlet Boundary Condition," *AIAA Journal*, Vol. 30, No. 3, 1992, pp. 697–702.

[4] Anon., "VSAERO Users' Manual Revision E.4," Analytical Methods Inc., Redmond, WA, April 1993.

Comparison of Finite Element and Finite Volume Methods for Incompressible Viscous Flows

K. Nakajima* and Y. Kallinderis†
University of Texas at Austin,
Austin, Texas 78712

I. Introduction

FINITE element and finite volume methods are widely used as general appoximation methods in the area of computational fluid dynamics. A direct comparison between the two approaches

---

Received June 17, 1993; revision received Oct. 12, 1993; accepted for publication Oct. 12, 1993.

*Graduate Research Assistant; currently at Department of Aerospace Engineering and Engineering Mechanics, Mitsubishi Research Institute, Inc., Japan.

†Associate Professor. Member AIAA.

using specially designed test cases can show some of the strengths and weaknesses of each method.

According to the finite element method, the flow variables are approximated at points by linear combinations of known shape functions. The functions can be quite general, with varying degrees of continuity at the interelement boundaries. They are locally defined polynomials within each element. A special integral formulation of the governing equations is considered, called the weak formulation. This formulation employs weighting functions that multiply the residual. Assigning the weights to be unity, the basic finite volume formulation is recovered. The finite volume method can be derived from the conservation principles of fluid flow. It expresses conservation of mass and momentum within each grid cell.

The present work compares a Galerkin finite element scheme and a finite volume method of central-differencing type. Nonuniform grids are employed to test the accuracy and stability of the two methods. The unsteady Navier-Stokes equations of incompressible flow in two dimensions are considered.[1,2] The momentum equations combined with a pressure correction equation are solved employing a nonstaggered grid where all of the dependent variables are defined at the cell vertices. The test cases employed are flat-plate flows for which analytical results exist.

II. Spatial Discretizations

The governing equations are the two-dimensional Navier-Stokes equations of incompressible flow. An explicit/implicit marching scheme is adopted for integration in time. The velocity values are treated explicitly, while the pressure values are treated implicitly in the momentum equations. The velocity values are marched in time with a forward Euler scheme.[1] The continuity equation is formulated implicitly with the velocity values considered at time level $(n + 1)$.

The momentum equations can be written in the following conservation form:

$$\frac{\partial \boldsymbol{U}}{\partial t}+\frac{\partial \boldsymbol{F}}{\partial x}+\frac{\partial \boldsymbol{G}}{\partial y}=\frac{\partial \boldsymbol{R}}{\partial x}+\frac{\partial \boldsymbol{S}}{\partial y} \tag{1}$$

where

$$\boldsymbol{U}^T = [u, v], \quad \boldsymbol{F}^T = [u^2+p, uv], \quad \boldsymbol{G}^T = [uv, v^2+p]$$

$$\boldsymbol{R}^T = \frac{1}{Re}\left[\frac{\partial u}{\partial x}, \frac{\partial v}{\partial x}\right], \quad \boldsymbol{S}^T = \frac{1}{Re}\left[\frac{\partial u}{\partial y}, \frac{\partial v}{\partial y}\right]$$

and Re is the Reynolds number.

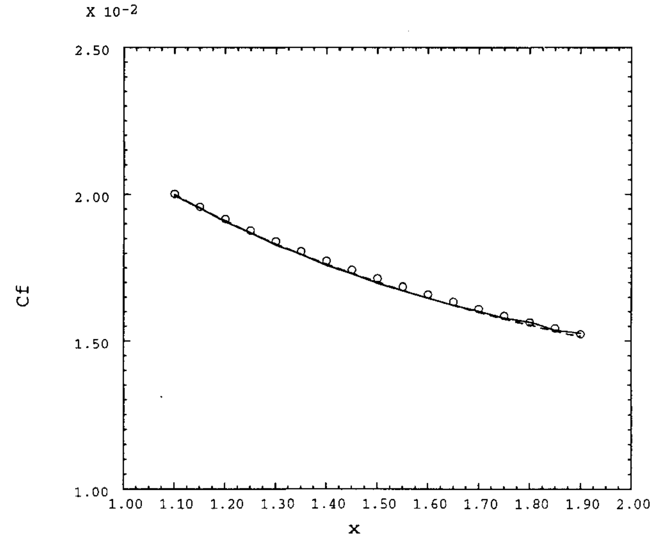

Fig. 1 Comparison of skin-friction distributions for Blasius boundary layer with $Re = 10^3$ (uniform grid). ——: FEM; – –: FVM; and o: Blasius.

A weak formulation is defined using a weighting function W as follows:

$$\int_{\Omega_e}\frac{\partial \boldsymbol{U}}{\partial t}W\,\mathrm{d}\Omega+\int_{\Omega_e}\frac{\partial \boldsymbol{F}}{\partial x}W\,\mathrm{d}\Omega+\int_{\Omega_e}\frac{\partial \boldsymbol{G}}{\partial y}W\,\mathrm{d}\Omega$$

$$=\int_{\Omega_e}\frac{\partial \boldsymbol{R}}{\partial y}W\,\mathrm{d}\Omega+\int_{\Omega_e}\frac{\partial \boldsymbol{S}}{\partial y}W\,\mathrm{d}\Omega \tag{2}$$

where Ω_e is the area of each element.

A. Galerkin Finite Element Method

In Eq. (2), the state and flux vectors are approximated as

$$\boldsymbol{U}=\sum_j N_j\boldsymbol{U}_j, \quad \boldsymbol{F}=\sum_j N_j\boldsymbol{F}_j, \quad \boldsymbol{G}=\sum_j N_j\boldsymbol{G}_j$$

$$\boldsymbol{R}=\sum_j N_j\boldsymbol{R}_j, \quad \boldsymbol{S}=\sum_j N_j\boldsymbol{S}_j$$

where the subscript j denotes the values at each cell corner. According to the Galerkin approach, we consider $W = N_i$. Integrating by parts Eq. (2), we get the following integral equation:

$$\frac{\mathrm{d}\boldsymbol{U}_j}{\mathrm{d}t}\int_{\Omega_e}N_iN_j\,\mathrm{d}\Omega+\boldsymbol{F}_j\int_{\Omega_e}N_i\frac{\partial N_j}{\partial x}\,\mathrm{d}\Omega+\boldsymbol{G}_j\int_{\Omega_e}N_i\frac{\partial N_j}{\partial y}\,\mathrm{d}\Omega$$

$$=-\boldsymbol{U}_j\int_{\Omega_e}\frac{1}{Re}\left(\frac{\partial N_i}{\partial x}\frac{\partial N_j}{\partial x}+\frac{\partial N_i}{\partial y}\frac{\partial N_j}{\partial y}\right)\mathrm{d}\Omega+\oint_{\Gamma}N_j\boldsymbol{q}\,\mathrm{d}\Gamma \tag{3}$$

where Γ is the domain boundary and $\boldsymbol{q}$ is the value of the state vector at the boundary. All of the terms in the integrands in Eq. (3) are evaluated numerically using Gauss-Legendre quadrature. In the present work, bilinear interpolation functions (N_j) are employed to compare the method to a classical central-type difference finite volume scheme that is second-order accurate in space.

B. Finite Volume Method

Applying the weighting function $W = 1$ to Eq. (2), and integrating over the area of a cell using Green's theorem, it is obtained

$$\frac{\mathrm{d}}{\mathrm{d}t}\int_{\Omega_e}\boldsymbol{U}\,\mathrm{d}\Omega+\oint_{\Gamma_e}(\boldsymbol{F}\,\mathrm{d}y-\boldsymbol{G}\,\mathrm{d}x)=\oint_{\Gamma_e}(\boldsymbol{R}\,\mathrm{d}y-\boldsymbol{S}\,\mathrm{d}x) \tag{4}$$

where Γ_e is the boundary of the element domain Ω_e. The line integrals in Eq. (4) represent the fluxes across the cell edges and are computed via the midpoint integration rule, as follows;

$$\frac{\Delta \boldsymbol{U}_c}{\Delta t}S_{\Omega_e}=-\sum_{e=1}^{4}(\boldsymbol{F}_e\Delta y_e-\boldsymbol{G}_e\Delta x_e)+\sum_{e=1}^{4}(\boldsymbol{R}_e\Delta y_e-\boldsymbol{S}_e\Delta x_e) \tag{5}$$

where $\boldsymbol{F}_e$, $\boldsymbol{G}_e$, $\boldsymbol{R}_e$, and $\boldsymbol{S}_e$ denote the flux vectors at the midpoint of the cell edges. Also, S_{Ω_e} is the cell area and Δx_e, Δy_e are the edge projections in the x and y directions, respectively. The flux vectors at the midpoint of the cell edges are obtained as average of the values at the edge endpoints (central-type differencing).

III. Comparison of Methods

The CPU time on an IBM Risc/6000 for solving the momentum equations is 1.20×10^{-4} s/cell/step for the finite element method (FEM), while it is 1.33×10^{-4} s/cell/step for the finite volume method (FVM). The required memory storage is 94 words/cell for FEM and 41 words/cell for FVM.

Uniform Grid

A Blasius boundary-layer case is calculated with an inlet Reynolds number of 10^3. An orthogonal grid of 41×73 points is em-

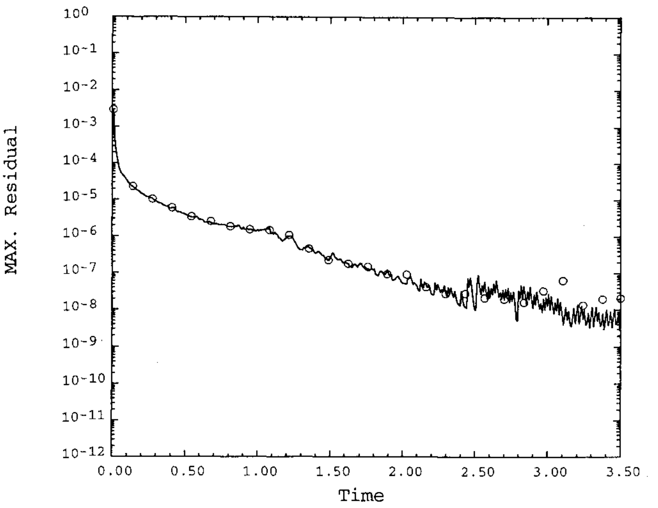

Fig. 2 Convergence history for Blasius boundary layer with $Re = 10^3$ (uniform grid). ——: FEM and o: FVM.

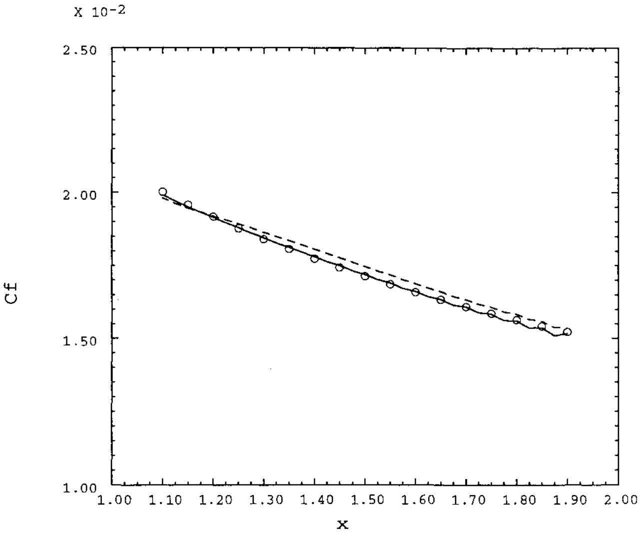

Fig. 3 Effect of grid stretching on skin-friction distributions for Blasius boundary layer with $Re = 10^3$ (grid with 50% stretching). ——: FEM; – –: FVM; and o: Blasius.

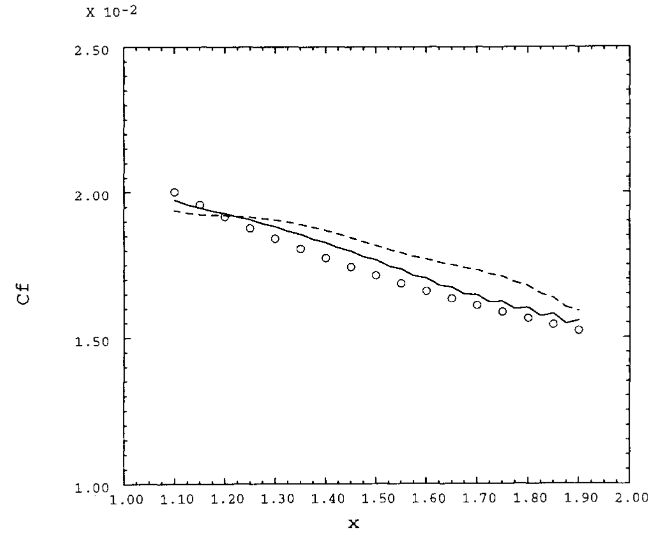

Fig. 4 Effect of grid stretching on skin-friction distributions for Blasius boundary layer with $Re = 10^3$ (grid with 70% stretching). ——: FEM; – –: FVM; and o: Blasius.

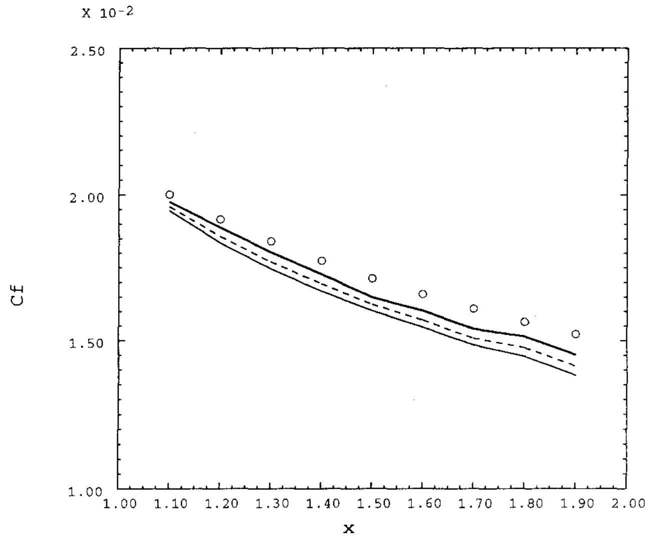

Fig. 5 Effect of smoothing on accuracy of the FEM. Skin-friction distributions for Blasius boundary layer with $Re = 10^3$. ——: $\sigma_4 = 1.0 \times 10^{-3}$; – –: 2.0×10^{-3}; ——: 3.0×10^{-3}; and o: Blasius.

ployed. The smallest grid normal spacing of 0.004 is applied at the wall and a constant grid stretching factor of 1.10 was employed in the normal to the surface direction.

Figure 1 shows comparison of computed skin-friction distributions at the wall with that from the analytical Blasius solution. Both the FEM and FVM results agree very well with the Blasius analytical solution. Figure 2 presents the convergence history of both methods via the maximum residual of velocity. The two convergence histories are similar.

Nonuniform Grid

Larger values of the grid stretching factor (f_s) are employed here. These are $f_s = 1.50$ and 1.70. Figure 3 shows comparison of computed skin-friction distributions at the wall with that from the analytical Blasius solution for $f_s = 1.50$. The FEM and FVM solutions agree very well with the Blasius analytical solutions except for small oscillations. Figure 4 shows comparison of computed skin-friction distributions at the wall with that from the analytical Blasius solution for $f_s = 1.70$. Accuracy of both the FEM and FVM is affected by the relatively large grid stretching. However, the finite element result is more accurate than the finite volume.

Effect of Smoothing

The effect of the fourth-order smoothing terms on accuracy of both methods is examined. Blasius boundary-layer cases are calculated with an inlet Re of 10^3. A grid of 11 × 19 points is employed. The smallest grid normal spacing of 0.016 is applied at the wall and a constant grid stretching factor of 1.10 was employed in the normal to the surface direction. A low value of the Re is considered so that the magnitude of the artificial viscosity term is not dominant over the magnitude of the physical viscous term.

Three different values of σ_4 are applied for both methods. These are 1.0×10^{-3}, 2.0×10^{-3}, and 3.0×10^{-3}, respectively. Figure 5 shows the computed skin-friction distributions at the wall for the finite element case. It shows that the smoothing terms deteriorate the numerical accuracy. The larger the value of the smoothing coefficient, the further away the numerical solution gets from the analytical one. The effect of increasing the amount of smoothing is very similar for the finite volume method, as well.

IV. Concluding Remarks

A Galerkin finite element method that employs bilinear interpolation functions, as well as a central-type differencing finite volume scheme that employs linear interpolations, were compared in terms of accuracy, stability, and computing requirements. Two were the points of comparisons; 1) sensitivity to grid quality and 2) effect of artificial dissipation.

The two methods were stable and equally accurate with uniform grid. The finite element method was found to be less sensitive to grid nonuniformity for the cases considered. Finally, the FEM and FVM required approximately the same amount of computing time per cell per step. However, the amount of required memory storage was more than double for the FEM.

Acknowledgment

This work is supported by the NSF Engineering Research Centers program Grant CDR-8721512.

References

[1] Kallinderis, Y., and Nakajima, K., "A Finite-Element Method for the Incompressible Navier-Stokes Equations with Adaptive Hybrid Grids," AIAA Paper 93-3005, July 1993.

[2] Nakajima, K., "Incompressible Navier-Stokes Methods with Hybrid Adaptive Grids," M. S. Thesis, Dept. of Aerospace Engineering and Engineering Mechanics, Univ. of Texas at Austin, TX, May 1993.

Practical Formulation of a Positively Conservative Scheme

Shigeru Obayashi*
NASA Ames Research Center,
Moffett Field, California 94035
and
Yasuhiro Wada†
NASA Lewis Research Center, Cleveland, Ohio 44135

Introduction

APPROXIMATE Riemann solvers have been highly successful for computing the Euler/Navier-Stokes equations, but linearized Riemann solvers are known to fail occasionally by predicting non-physical states with negative density or internal energy. Positively conservative schemes, in contrast, guarantee physical solutions from realistic input. The Harten-Lax-van Leer-Einfeldt (HLLE) scheme is a typical example of a positively conservative scheme.[1] However, the HLLE scheme is highly dissipative at contact discontinuities and shear layers and thus it is not applicable to practical simulations. An existing modification to the HLLE scheme, known as HLLEM, enhances the resolution to that of the Roe scheme.[2] However, this modification violates the positivity of density and internal energy. Precise derivation of the modification yields a quadratic inequality and thus requires a case-by-case treatment.[3] This Note describes a new, modified HLLE scheme that satisfies the positively conservative condition approximately. Sample computations are included to demonstrate the resolution and the robustness of the scheme.

Algorithm Development

For brevity, the Euler equations are limited to one Cartesian space dimension. The conservation form of the equation is

$$Q_t + F_x = 0 \tag{1a}$$

where the conserved quantities Q and flux F are

$$Q = \begin{pmatrix} \rho \\ \rho u \\ e \end{pmatrix}, \qquad F = \begin{pmatrix} \rho u \\ \rho u^2 + p \\ (e+p)\,u \end{pmatrix} \tag{1b}$$

and where ρ is the density, u is the velocity, and e is the total energy per unit volume. The pressure p is related to the conserved quantities through the equation of state for a perfect gas:

$$p = (\gamma - 1)(e - \rho u^2/2) \tag{1c}$$

The cell interface flux F_{LR} can be evaluated by the HLLE scheme[1] as

$$F_{LR} = 1/2(F_L + F_R - \bar{R}\hat{\Lambda}\bar{L}\Delta Q) \tag{2a}$$

where

$$\Delta Q = Q_R - Q_L \tag{2b}$$

$$\hat{\Lambda} = (b_R^+ + b_L^-)/(b_R^+ - b_L^-)\,\bar{\Lambda} - 2(b_R^+ b_L^-)/(b_R^+ - b_L^-)I \tag{2c}$$

$$\bar{\Lambda} = \begin{pmatrix} \bar{u} & & 0 \\ & \bar{u} + \bar{c} & \\ 0 & & \bar{u} - \bar{c} \end{pmatrix} \tag{2d}$$

and where $\bar{R}$, $\bar{\Lambda}$, and $\bar{L}$ are the right eigenvector, eigenvalue, and left eigenvector matrices, respectively, of the Roe-averaged Jacobian,[4] I is the identity matrix, and the subscripts L and R indicate the left and right states. The HLLE scheme defines b_R^+ and b_L^- as

$$b_R^+ = \max(\bar{u} + \bar{c}, u_R + c_R, 0) \tag{3a}$$

$$b_L^- = \min(\bar{u} - \bar{c}, u_L - c_L, 0) \tag{3b}$$

This scheme satisfies all of the stability, entropy, and positively conservative conditions required for the nonlinear difference equations.[1–3] Numerical dissipation determined by b_R^+ and b_L^- could still be reduced under the stability and positively conservative conditions.[1] However, the resulting scheme would violate the entropy condition[3] and thus it is not used here.

The HLLE scheme approximates the solution of the Riemann problem with two waves propagating with speed of $b_R = \max(\bar{u} + \bar{c}, u_R + c_R)$ and $b_L^- = \min(\bar{u} - \bar{c}, u_L - c_L)$ and a state Q_{LR} between those waves. Comparing with the Roe scheme, the HLLE scheme introduces large numerical dissipation to contact discontinuities.[1] The modified HLLE (HLLEM) scheme exhibits a similar resolution to the Roe scheme,[1] but the resulting scheme violates the positively conservative condition.[3] A new modification[3] which satisfies the positively conservative condition is obtained by replacing the state Q_{LR} with

$$\tilde{Q}_{LR} = \begin{cases} Q_{LR} - \delta\bar{B}\Delta Q, & \text{for} \quad x/t < (b_L + b_R)/2 \\ Q_{LR} + \delta\bar{B}\Delta Q, & \text{for} \quad x/t > (b_L + b_R)/2 \end{cases} \tag{4a}$$

where

$$Q_{LR} = [b_R Q_R - b_L Q_L - (F_R - F_L)]/(b_R - b_L) \tag{4b}$$

and

$$\bar{B}\Delta Q = \bar{R}\begin{pmatrix} 1 & & \\ & 0 & \\ & & 0 \end{pmatrix}\bar{L}\Delta Q = \frac{\bar{c}^2\Delta\rho - \Delta p}{\bar{c}^2}\begin{pmatrix} 1 \\ \bar{u} \\ \bar{u}^2/2 \end{pmatrix} \tag{4c}$$

Received Aug. 31, 1993; accepted for publication Oct. 13, 1993. Copyright © 1993 by the American Institute of Aeronautics and Astronautics, Inc. No copyright is asserted in the United States under Title 17, U.S. Code. The U.S. Government has a royalty-free license to exercise all rights under the copyright claimed herein for Governmental purposes. All other rights are reserved by the copyright owner.

*Senior Research Scientist, MCAT Institute. Senior Member AIAA.

†Institute for Computational Mechanics in Propulsion; currently at Computational Sciences Division, National Aerospace Laboratory, Tokyo, Japan. Member AIAA.